

Exceptionally increased reversible capacity of O3-type NaCrO₂ cathode by preventing irreversible phase transition



Wonseok Ko^a, Min-Kyung Cho^b, Jungmin Kang^a, Hyunyoung Park^a, Jinho Ahn^a, Yongseok Lee^a, Seokjin Lee^a, Sangyeop Lee^a, Kwang Heo^c, Jihyun Hong^d, Jung-Keun Yoo^e, Jongsoo Kim^{a,*}

^a Department of Energy Science, Sungkyunkwan University, Suwon 440-746, Republic of Korea

^b Advanced Analysis Center, Korea Institute of Science and Technology (KIST), 14 Gil 5 Hwarang-ro, Seongbuk-gu, Seoul 02792, Republic of Korea

^c Department of Nanotechnology and Advanced Materials Engineering, Sejong University, Seoul 05006, Republic of Korea

^d Energy Materials Research Center, Korea Institute of Science and Technology (KIST), 14 Gil 5 Hwarang-ro, Seongbuk-gu, Seoul 02792, Republic of Korea

^e Carbon Composites Department, Composites Research Division, Korea Institute of Materials Science (KIMS), 797 Changwondaero, Changwon, Republic of Korea

ARTICLE INFO

Keywords:

Na-ion batteries
Cathode
Cation migration
Reversible
First-principles calculation

ABSTRACT

Although O3-type NaCrO₂ has various merits as a promising cathode material for Na-ion batteries, only ~0.5 mol Na⁺ in O3-type NaCrO₂ can be used because of irreversible phase transition by Cr migration to the Na layers. Thus, it is important to increase the Na⁺ content that can be reversibly de/intercalated by O3-type NaCrO₂. Through combined studies using first-principles calculation and experiments, we demonstrate that the presence of Sb⁵⁺ in the NaCrO₂ structure can suppress Cr migration even after charging to 4.1 V (vs. Na⁺/Na) and enables an increase in the Na content that can be reversibly de/intercalated. During charge/discharge at C/20 (1C = 175 mA g⁻¹), O3-type Na_{0.72}Cr_{0.86}Sb_{0.14}O₂ delivers a specific capacity of ~175 mAh g⁻¹ corresponding to ~0.72 mol Na⁺ de/intercalation, representing highly enhanced electrochemical performance compared with that of O3-type NaCrO₂, which exhibits poor coulombic efficiency of only ~37% under the same conditions.

1. Introduction

With increasing concerns over the environmental pollution resulting from the use of fossil fuels, many researchers have focused on the development of not only renewable and eco-friendly energy sources but also efficient energy storage systems (ESSs) [1,2]. Li-ion batteries (LIBs) have received considerable attention as one of the most promising ESSs because of their high energy and stable cycle life [1–6]. Their application has thus expanded from small electronic devices to large-scale ESSs such as electric vehicles (EVs) [7–9]. Despite the undeniable merits of LIBs, the limited Li resources in the Earth's crust is considered a major drawback in terms of satisfying the accelerating demand for LIBs for grid-scale ESSs, preventing their further application [10–15].

Recently, Na-ion batteries (NIBs) have attracted attention as potential alternatives to LIBs for large-scale application because of the essentially unlimited Na resources as well as the monovalent-ion-based reaction mechanism similar to that of LIBs [16–21]. In particular, layered-type oxide materials Na_xTMO₂ (TM: transition metals) have been intensively studied as promising cathode materials for NIBs owing to their notable merits such as the large gravimetric energy density and small molar mass and the large two-dimensional ionic pathways for fast Na⁺ diffusion [22–26]. O3-type NaCrO₂ (O3-NaCrO₂) is also consid-

ered an attractive layered-oxide cathode for NIBs because of its large theoretical capacity of ~250 mAh g⁻¹, corresponding to ~1 mol Na⁺ de/intercalation [27]. In real operation under the NIB system, however, it was reported that only ~0.5 mol Na⁺ in O3-NaCrO₂ can be reversibly de/intercalated in the structure with phase transition between the O3 and P3 phases, indicating that the available specific capacity of O3-NaCrO₂ is only ~120 mAh g⁻¹ [22,27]. During further Na⁺ deintercalation from O3-Na_{0.5}CrO₂, Cr ions are moved to Na layers and Na_xCrO₂ undergoes irreversible phase transition, preventing facile Na⁺ intercalation into Na layers and causing the poor cycle-performance of O3-NaCrO₂ [27]. Thus, suppression of the irreversible Cr migration to the Na layers to enhance the electrochemical performance of O3-NaCrO₂ is important and has been investigated in several studies.

Herein, we demonstrate that Sb substitution in the O3-Na_xCrO₂ structure can successfully suppress the Cr migration to Na layers. Furthermore, more than 0.14 mol Sb substitution in the structure enables reversible ~0.72 mol Na⁺ deintercalation in the Na_xCrO₂ structure during charging to 4.1 V without irreversible phase transition and oxidation to Cr⁶⁺. Through electrochemical tests at a current density of C/20 (1C = 175 mA g⁻¹), it was verified that the O3-Na_{0.72}Cr_{0.86}Sb_{0.14}O₂ delivers a large specific capacity of ~175 mAh g⁻¹ with a high initial coulombic efficiency of above 98.7%. The com-

* Corresponding author.

E-mail address: jongsoo.kim@skku.edu (J. Kim).

bined studies using first-principles calculation, *operando* X-ray diffraction (XRD), and *ex-situ* high-angle annular dark-field scanning transmission electron microscopy (HAADF-STEM) indicate that Cr ions in the O3-Na_{0.72}Cr_{0.86}Sb_{0.14}O₂ structure did not migrate to Na layers even after full deintercalation of ~0.72 mol Na⁺ and that only reversible O3–P3 phase transition was observed without any irreversible phase deformation by Cr migration to Na layers during charging to 4.1 V (vs. Na⁺/Na). Furthermore, even at 5C, a specific capacity of ~124 mAh g⁻¹ was maintained by O3-Na_{0.72}Cr_{0.86}Sb_{0.14}O₂, corresponding to ~71.31% of the capacity measured at C/20. In terms of cyclability, O3-Na_{0.72}Cr_{0.86}Sb_{0.14}O₂ exhibited a capacity retention of ~78.64% for 200 cycles at 2C. These electrochemical properties indicate the outstanding power-capability and cyclability of O3-Na_{0.72}Cr_{0.86}Sb_{0.14}O₂ as a promising cathode material for NIBs.

2. Results and discussion

2.1. Crystal structure and morphology of O3-Na_{0.72}Cr_{0.86}Sb_{0.14}O₂

O3-Na_{0.72}Cr_{0.86}Sb_{0.14}O₂ was successfully synthesized via the conventional solid-state method [28] and the detailed synthetic procedures and crystal structure information are arranged in the supporting information. To investigate the structural information of O3-Na_{0.72}Cr_{0.86}Sb_{0.14}O₂, we performed XRD analyses with Rietveld refinement. Fig. 1a shows that O3-Na_{0.72}Cr_{0.86}Sb_{0.14}O₂ with *R*3̄m space group was prepared without any impurities or second phases, and its lattice parameters are *a* (= *b*) = 2.96598(9) Å, *c* = 16.2099(8) Å, and *V* = 123.494(8) Å³. Detailed structural information for O3-Na_{0.72}Cr_{0.86}Sb_{0.14}O₂ including the atomic coordinates, thermal factor, and occupancy are tabulated in Table S1. The low reliability factors (*R*_p: 3.74%, *R*_f: 2.35%, *χ*²: 1.33%, *R*_F: 8.26%) indicate the high accuracy of the Rietveld refinement result. The morphology and atomic composition of O3-Na_{0.72}Cr_{0.86}Sb_{0.14}O₂ were verified by transmission electron microscopy (TEM) analyses combined with energy-dispersive X-ray spectroscopy (EDS) for elemental mapping. As shown in Fig. 1b, the Na, Cr, and Sb elements were homogeneously distributed in O3-Na_{0.72}Cr_{0.86}Sb_{0.14}O₂ particles with an average size of ~500 nm. Moreover, the TEM–EDS mapping analyses indicate that the elemental ratio in the O3-Na_{0.72}Cr_{0.86}Sb_{0.14}O₂ particles is Na:Cr:Sb = ~0.721:~0.859:0.14, which is consistent with the inductively coupled plasma (ICP) spectroscopy results (Table S2). It was also verified that the oxidation state of Cr ions in O3-Na_{0.72}Cr_{0.86}Sb_{0.14}O₂ was nearly +3, which indicates that Na ions can be de/intercalated through Cr³⁺/Cr⁴⁺ redox reaction (Fig. S1). In addition, we performed bond-valence energy landscape (BVEL) analyses based on the structural information of O3-Na_{0.72}Cr_{0.86}Sb_{0.14}O₂ [29–31]. As shown in Fig. 1c and d, it was predicted that there are sufficiently large two-dimensional spaces for facile and smooth Na⁺ diffusion between interlayers composed of (Cr, Sb)O₆ octahedra.

2.2. Change of electrochemical behavior of O3-Na_xCr_{1-x}Sb_xO₂ as a function of Sb content

To investigate the effect of Sb substitution on the available capacity of O3-NaCrO₂ without severe irreversible reaction related to Cr migration, we compared the electrochemical properties of O3-Na_{1-2x}Cr_{1-x}Sb_xO₂ (*x* = 0, 0.09, and 0.14). Fig. 2a presents the initial charge/discharge profiles of Na_{0.72}Cr_{0.86}Sb_{0.14}O₂ at the current rate of C/20 (1C = 175 mA g⁻¹) in the voltage range between 1.5 and 4.1 V (vs. Na⁺/Na). It was verified that more than 0.14 mol Sb substitution in the O3-NaCrO₂ structure results in a highly improved initial coulombic efficiency of ~98.7%. In terms of the initial discharge capacity of O3-Na_{0.72}Cr_{0.86}Sb_{0.14}O₂, it is ~2.16 and ~1.40 times higher than those of O3-Na_{0.82}Cr_{0.91}Sb_{0.09}O₂ and O3-NaCrO₂ under same condition, respectively (Fig. 2b and c). In particular, the initial coulombic efficiency of O3-NaCrO₂ was only ~37.04%. These electrochemi-

cal results indicate that more than 0.14 mol Sb substitution can result in an increase of the reversibly available Na content in the O3-Na_{1-2x}Cr_{1-x}Sb_xO₂ structure during charging to 4.1 V (vs. Na⁺/Na). However, it was verified that less than 0.1 mol Sb substitution in the O3-NaCrO₂ structure does not greatly improve the electrochemical performance, which agrees well with previous research [32]. In addition, Fig. S2–3 and Table S3–5 present scanning electron microscopy (SEM) images, XRD patterns and ICP spectroscopy results of the O3-NaCrO₂ and O3-Na_{0.82}Cr_{0.91}Sb_{0.09}O₂ samples, which show that all the samples exhibit not only similar particle sizes and morphologies but also consistent crystal structures without any impurities or second phases. These results imply that the only differences in the electrochemical performance originate from the substituted Sb content in the structure. Thus, we speculated that the greatly enhanced electrochemical performance of O3-NaCrO₂ by 0.14 mol Sb substitution resulted from reversible phase transition during charge/discharge even after charging to 4.1 V (vs. Na⁺/Na) by the suppression of not only Cr migration to Na layers but also oxidation to Cr⁶⁺. In addition, we prepared the 0.18 mol Sb-substituted Na_{0.64}Cr_{0.82}Sb_{0.18}O₂ phase using the same synthesis process for O3-Na_{0.72}Cr_{0.86}Sb_{0.14}O₂. As presented in Fig. S4, it was verified that the Na_{0.64}Cr_{0.82}Sb_{0.18}O₂ phase is composed of mixed O3-type and P2-type layered structure, not the pure O3-type layered structure, which is consistent with the formation of P2-type layered structure at the low Na contents (below ~0.67 mol) in Na[TM]O₂ [33,34]. Especially, Fig. S5 shows that the electrochemical performances of Na_{0.64}Cr_{0.82}Sb_{0.18}O₂ were poorer than those of O3-Na_{0.72}Cr_{0.86}Sb_{0.14}O₂. These results indicate that the Na_{1-2x}Cr_{1-x}Sb_xO₂ phases with more than 0.14 mol Sb in the structure exhibit not only formation of P2/O3 biphasic structure but also relatively poor electrochemical properties compared to those of O3-Na_{0.72}Cr_{0.86}Sb_{0.14}O₂.

2.3. Reversible structural change of Na_xCr_{0.86}Sb_{0.14}O₂ during charge/discharge

To predict the theoretical electrochemical properties of Na_{0.72}Cr_{0.86}Sb_{0.14}O₂ and the effect of Sb substitution in the structure, the cluster expansion method of first-principles calculation was applied. Using CASM software, we calculated the formation energy of various states as a function of the Na-ion content in O3- and P3-Na_xCr_{0.86}Sb_{0.14}O₂ (0 ≤ *x* ≤ 1) using the following equation:

$$V = - \frac{E[\text{Na}_{x_2}\text{Cr}_{0.86}\text{Sb}_{0.14}\text{O}_2] - E[\text{Na}_{x_1}\text{Cr}_{0.86}\text{Sb}_{0.14}\text{O}_2] - (x_2 - x_1)E[\text{Na}]}{(x_2 - x_1)F}$$

In the above equation, *V* represents the average redox potential depending on the Na-ion content in Na_xCr_{0.86}Sb_{0.14}O₂ (*x*₁ ≤ *x* ≤ *x*₂), *E*[Na_xCr_{0.86}Sb_{0.14}O₂] is the calculated formation energy for the most stable configurations of each composition (0 ≤ *x* ≤ 1), *E*[Na] is the Na metal energy, and *F* is the Faraday constant. Fig. 3a presents the convex-hull plot on the formation energies of various O3- and P3-Na_xCr_{0.86}Sb_{0.14}O₂ configurations. It was verified that reversible ~0.72 mol Na⁺ de/intercalation can occur in the Na_xCr_{0.86}Sb_{0.14}O₂ structure in the available voltage range between 1.5 and 4.1 V (vs. Na⁺/Na). In particular, after further Na⁺ deintercalation from the Na_{0.25}Cr_{0.86}Sb_{0.14}O₂ structure, the P3 phase is more stable than the O3 phase, indicating the occurrence of the O3/P3 phase transition during charge/discharge. The predicted redox potentials of O3- and P3-Na_xCr_{0.86}Sb_{0.14}O₂ are consistent with the experimentally measured charge/discharge profiles (Fig. 3b).

The structure change of Na_xCr_{0.86}Sb_{0.14}O₂ during the first charge and discharge was confirmed through *operando* XRD (O-XRD) at a current of C/10 in the voltage range of 1.5–4.1 V (vs. Na⁺/Na). Fig. 3c shows that the XRD peaks such as (003), (006), (101), and (012) monotonously shifted during charge/discharge with a change in the peak intensities, indicating Na⁺ de/intercalation from/into the Na_xCr_{0.86}Sb_{0.14}O₂ structure. In particular, it was observed that

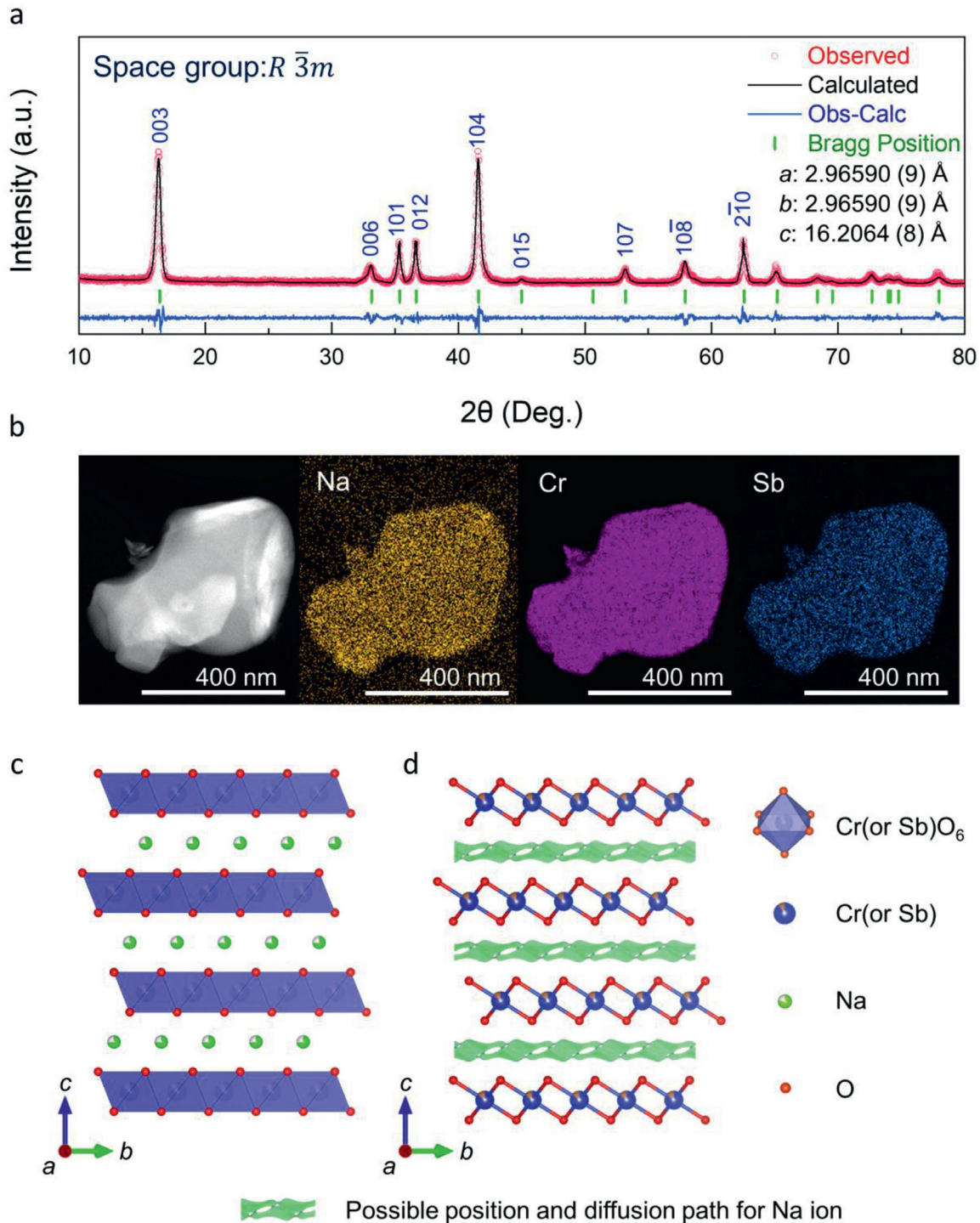


Fig. 1. (a) Rietveld refinement of XRD pattern of O3- $\text{Na}_{0.72}\text{Cr}_{0.86}\text{Sb}_{0.14}\text{O}_2$. (B) TEM-EDS mapping of O3- $\text{Na}_{0.72}\text{Cr}_{0.86}\text{Sb}_{0.14}\text{O}_2$. (C) Crystal structure of O3- $\text{Na}_{0.72}\text{Cr}_{0.86}\text{Sb}_{0.14}\text{O}_2$ and (D) 3D BVLE map with all possible positions and diffusion paths of Na ions.

$\text{Na}_x\text{Cr}_{0.86}\text{Sb}_{0.14}\text{O}_2$ experiences reversible O3/P3 phase transition during charge/discharge without the formation of the O3' phase, indicating irreversible Cr migration to Na layers. Moreover, the shift of the (003) and (006) peaks toward low 2θ angles during charge indicates enlargement of the c -lattice parameter by repulsion between O^{2-} ions after Na^+ deintercalation from the structure. This O -XRD results of O3- $\text{Na}_x\text{Cr}_{0.86}\text{Sb}_{0.14}\text{O}_2$ are consistent with the electrochemical results of the high initial coulombic efficiency and the computational results on the reversible O3/P3 phase transition. In terms of Na_xCrO_2 , however, the O -

XRD measurement clearly indicates the occurrence of irreversible multiple phase transitions among the O3, O'3, P'3, and O3' phases during charging to 4.1 V (vs. Na^+/Na) and greatly reduced XRD peak intensities (Fig. 3d), which is similar to previous research results on O3- NaCrO_2 [27]. We also calculated the variation of the c -lattice parameter of $\text{Na}_x\text{Cr}_{0.86}\text{Sb}_{0.14}\text{O}_2$ through Rietveld refinement based on the O -XRD patterns. As presented in Fig. 3e, the total difference of the c -lattice parameter between $\text{Na}_{0.72}\text{Cr}_{0.86}\text{Sb}_{0.14}\text{O}_2$ and $\text{Na}_0\text{Cr}_{0.86}\text{Sb}_{0.14}\text{O}_2$ was $\sim 4.20\%$. Moreover, after the initial charge/discharge, the c -lattice

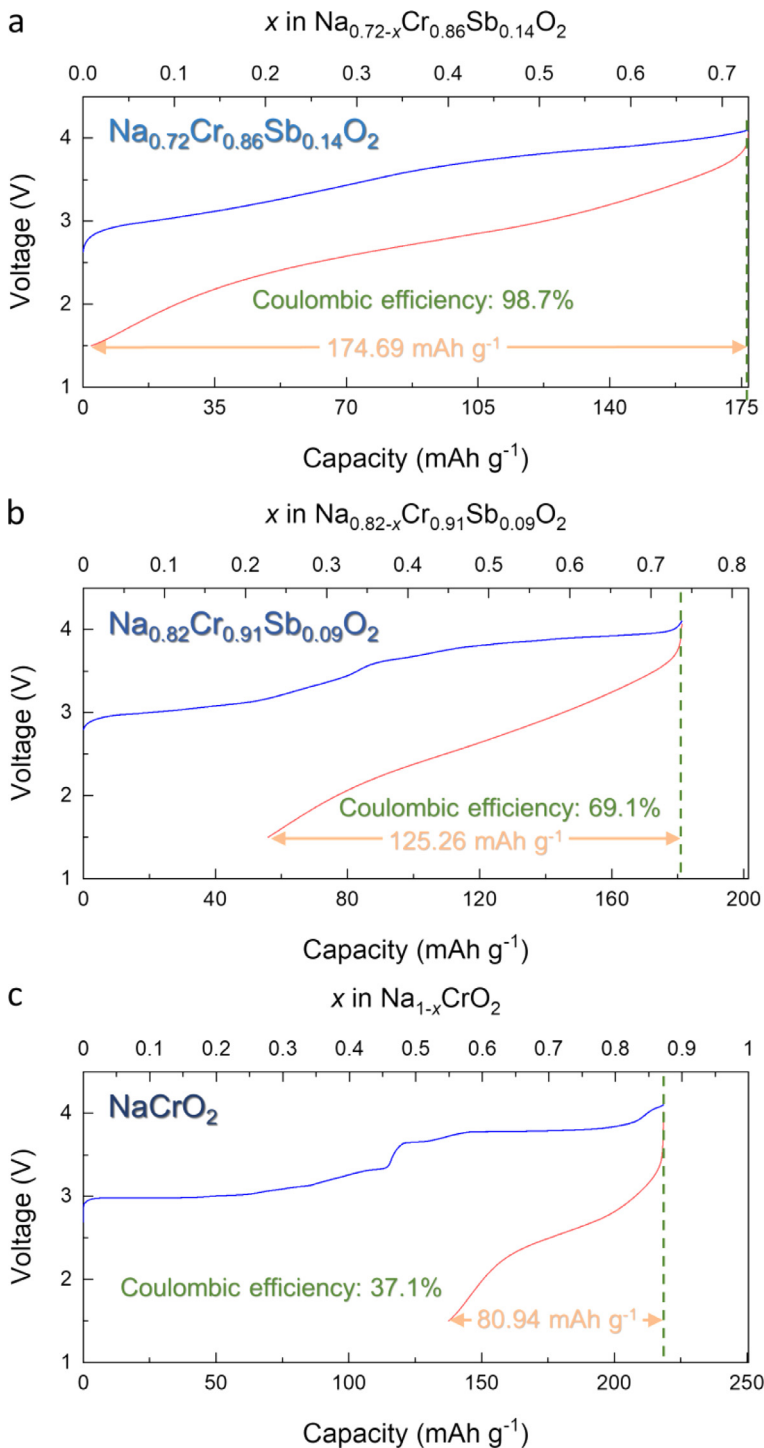


Fig. 2. Initial charge and discharge profile and coulombic efficiency of (a) O3-Na_{0.72}Cr_{0.86}Sb_{0.14}O₂, (b) O3-Na_{0.82}Cr_{0.91}Sb_{0.09}O₂, and (c) O3-NaCrO₂ in the voltage range of 1.5–4.1 V (vs. Na⁺/Na) at each C/20.

parameter returned to near the original value, 16.17 Å, which is another reason supporting the idea that O3-Na_{0.72}Cr_{0.86}Sb_{0.14}O₂ experiences a reversible structural change without Cr migration to the Na layers during cycling in the voltage range of 1.5–4.1 V (vs. Na⁺/Na).

HAADF-STEM analyses also provided direct evidence of the non-occurrence of Cr migration to the Na layers in the Na_{0.72}Cr_{0.86}Sb_{0.14}O₂ structure through visualization of atomic-scale crystal structures. The pristine states of O3-Na_{0.72}Cr_{0.86}Sb_{0.14}O₂ are composed of the general layered structure with the ABCABC stacking sequence along the *c*-direction (Fig. 4a). Moreover, after initial charge/discharge in the voltage range of 1.5–4.1 V (vs. Na⁺/Na), the crystal structure of O3-

Na_{0.72}Cr_{0.86}Sb_{0.14}O₂ was relatively retained under the same conditions without significant structural degradation or Cr migration (Fig. 4b) [27], which is clearly different from the HAADF-STEM results of O3-NaCrO₂ showing that the crystal structure of NaCrO₂ is totally deformed with Cr migration to the Na layers after 1 cycle unlike that of O3-Na_{0.72}Cr_{0.86}Sb_{0.14}O₂ (Fig. S6). In addition, we performed the HAADF-STEM and bright-field scanning transmission electron microscopy (BF-STEM) analyses of O3-Na_{0.72}Cr_{0.86}Sb_{0.14}O₂ and O3-NaCrO₂ electrodes for the various states, such as pristine, after cycling at difference charge cut-off voltages of 3.6 and 4.1 V (vs. Na⁺/Na). As shown in Fig. S7a, HAADF- and BF-STEM analyses indicate that pristine O3-

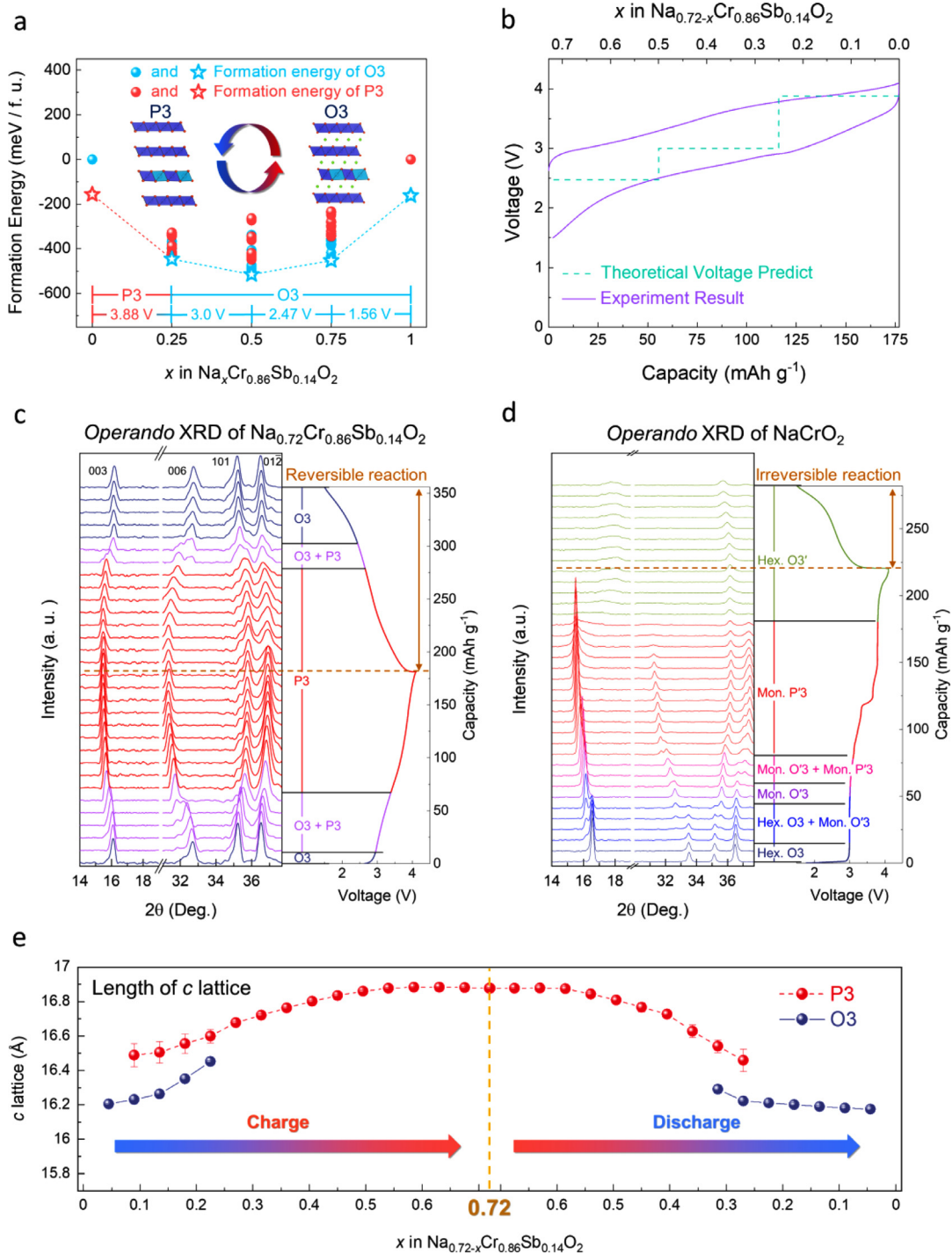


Fig. 3. (a) Formation energy of O3-type and P3-type Na_xCr_{0.86}Sb_{0.14}O₂ (0 ≤ x ≤ 1). (b) Cycle profile and predicted theoretical voltage of Na_xCr_{0.86}Sb_{0.14}O₂ (0 ≤ x ≤ 0.72) in the voltage range of 1.5–4.1 V (vs Na⁺/Na) at C/20. Operando XRD pattern of (c) Na_xCr_{0.86}Sb_{0.14}O₂ (voltage range: 1.5–4.1 V) and (d) NaCrO₂ (voltage range: 1.5–4.1 V). (e) changes in c lattice and structure according to the amount of Na ions in the structure of Na_xCr_{0.86}Sb_{0.14}O₂ (0 ≤ x ≤ 0.72).

Na_{0.72}Cr_{0.86}Sb_{0.14}O₂ is composed of the O3-type layered structure. Through the HAADF-Z contrast analysis, the intensity difference of Na and TM layers was clearly verified [35,36], and the c-lattice parameter measured by HAADF-Z contrast was well consistent with the Rietveld refinement results based on the XRD analyses (Fig. 1a). Moreover, the individual Sb and Cr elements was distinguished through the BF-Z contrast, since the BF intensity is determined by the atomic number and the atomic number of Sb is much larger than that of Cr [37]. After cycling at charge cut-off voltage of 3.6 and 4.1 V, the Cr migration to the Na layer

in the crystal structure of O3-Na_{0.72}Cr_{0.86}Sb_{0.14}O₂ was not occurred (Fig. S7b and c), and the *ex-situ* XRD analyses indicate that the crystal structure of O3-Na_{0.72}Cr_{0.86}Sb_{0.14}O₂ is well maintained without any irreversible transformation even at the high cut-off voltage of 4.1 V (Fig. S7d). Thus, it was confirmed that the O3-Na_{0.72}Cr_{0.86}Sb_{0.14}O₂ exhibited the high structural stability without any TM migration to the Na layers at the voltage range of 1.5–4.1 V. In terms of O3-NaCrO₂, it was clearly observed that the irreversible structure deformation was occurred during charging to 4.1 V (vs. Na⁺/Na). As shown in Fig. S8a and b, the pristine

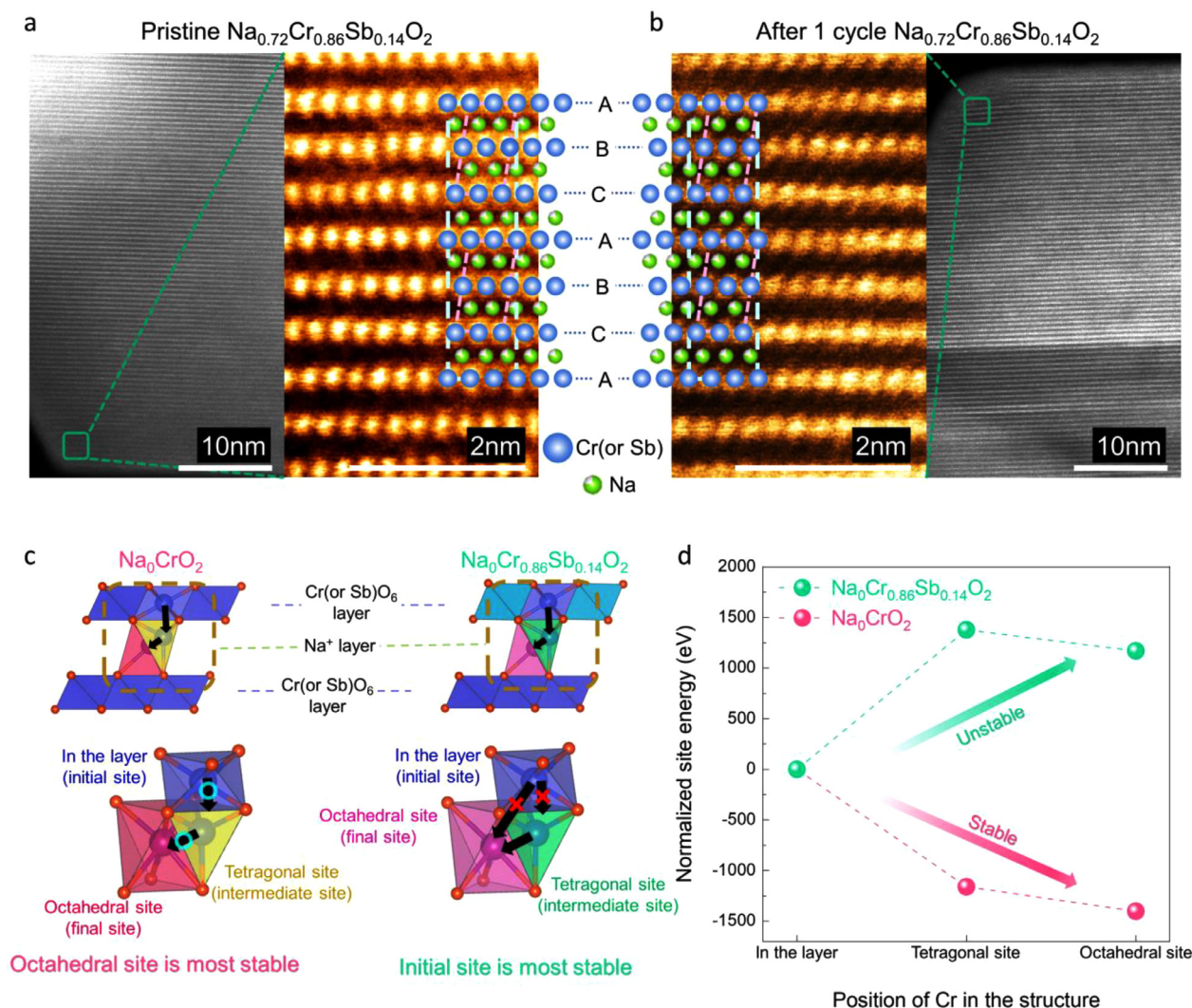


Fig. 4. HAADF-STEM analyses of (a) pristine $\text{Na}_{0.72}\text{Cr}_{0.86}\text{Sb}_{0.14}\text{O}_2$ and (b) 1-cycled $\text{Na}_{0.72}\text{Cr}_{0.86}\text{Sb}_{0.14}\text{O}_2$ prepared through charge/discharge in the voltage range of 1.5–4.1 V. (c) crystal structure of tetragonal and octahedral sites where Cr ions can migrate in O3- Na_0CrO_2 and O3- $\text{Na}_{0.72}\text{Cr}_{0.86}\text{Sb}_{0.14}\text{O}_2$. (d) comparison of formation energy as a function of the position of chromium ion in O3- Na_0CrO_2 and O3- $\text{Na}_{0.72}\text{Cr}_{0.86}\text{Sb}_{0.14}\text{O}_2$.

O3- NaCrO_2 and 1-cycled O3- NaCrO_2 with charge cut-off voltage of 3.6 V delivered the O3-type layered structure. After charging to 4.1 V, however, it was verified that the crystal structure of NaCrO_2 experienced the severe structural degradation by occurrence of stacking faults related to the Cr migration to Na-layers (Fig. S8c). These results are well matched the *ex-situ* XRD showing the irreversible phase-transition from O3-phase to O3'-phase after 1 cycle with the charge cut-off voltage of 4.1 V (Fig. S8d). Furthermore, we confirmed the difficulty of Cr migration to Na layers in the $\text{Na}_x\text{Cr}_{0.86}\text{Sb}_{0.14}\text{O}_2$ structure through first-principles calculation. Fig. 4c and d present a comparison of the theoretical pathways and the required energies for Cr migration to Na layers between pristine Na_0CrO_2 and $\text{Na}_{0.72}\text{Cr}_{0.86}\text{Sb}_{0.14}\text{O}_2$. In terms of Na_0CrO_2 , Cr migration to Na layers is thermodynamically stable; thus, the Cr ion in the CrO_6 layer in Na_0CrO_2 can be moved to the octahedral site via the tetragonal site, which interferes with Na^+ intercalation into the structure, and consequently, the electrochemical performance of pristine NaCrO_2 become poor after the Cr migration. However, the presence of Sb^{5+} ions in $\text{Na}_x\text{Cr}_{0.86}\text{Sb}_{0.14}\text{O}_2$ makes Cr migration to Na layers thermodynamically difficult, which enabled O3- $\text{Na}_{0.72}\text{Cr}_{0.86}\text{Sb}_{0.14}\text{O}_2$ to deliver a high initial coulombic efficiency of >98.7% even after charging to 4.1 V (vs. Na^+/Na), unlike O3- NaCrO_2 . We speculate that Sb^{5+} ions with high electronegativity and fixed valence state can enhance the structural stability during Na^+ de/intercalation from/into the $\text{Na}_x\text{Cr}_{0.86}\text{Sb}_{0.14}\text{O}_2$ structure,

preventing irreversible phase transition to the O3' phase and increasing the reversibly available capacity compared with that of NaCrO_2 .

2.4. Outstanding electrochemical performance and reaction mechanism of $\text{Na}_{0.72}\text{Cr}_{0.86}\text{Sb}_{0.14}\text{O}_2$

To confirm the power capability and cycle performance, we prepared an electrode using O3- $\text{Na}_{0.72}\text{Cr}_{0.86}\text{Sb}_{0.14}\text{O}_2$, and testing was conducted under various current density conditions in the voltage range of 1.5–4.1 V. As shown in Fig. 5a and b, O3- $\text{Na}_{0.72}\text{Cr}_{0.86}\text{Sb}_{0.14}\text{O}_2$ was continuously charged and discharged at various current densities of C/20, C/10, C/5, C/2, 1C, 2C, 3C, and 5C. At C/20, the specific charge and discharge capacities were 176.86 and 174.69 mAh g^{-1} , respectively, corresponding to reversible ~ 0.72 mol Na^+ de/intercalation from/into the structure. Additionally, we demonstrated cathodic and anodic electrochemical reaction of O3- $\text{Na}_{0.72}\text{Cr}_{0.86}\text{Sb}_{0.14}\text{O}_2$ in Na cell by cyclic voltammetry (CV) test (Fig. S9), showing the reversible $\text{Cr}^{3+}/\text{Cr}^{4+}$ redox reaction during charge/discharge. Even at 5C, O3- $\text{Na}_{0.72}\text{Cr}_{0.86}\text{Sb}_{0.14}\text{O}_2$ delivered a large discharge capacity of ~ 124.56 mAh g^{-1} , corresponding to $\sim 71.31\%$ of the capacity measured at C/20. Moreover, the specific capacity of O3- $\text{Na}_{0.72}\text{Cr}_{0.86}\text{Sb}_{0.14}\text{O}_2$ at 5C was ~ 4.4 and ~ 2.3 times higher than those of pristine O3- NaCrO_2 and O3- $\text{Na}_{0.88}\text{Cr}_{0.91}\text{Sb}_{0.09}\text{O}_2$ under the same conditions, respectively (Fig. S10). These results imply that

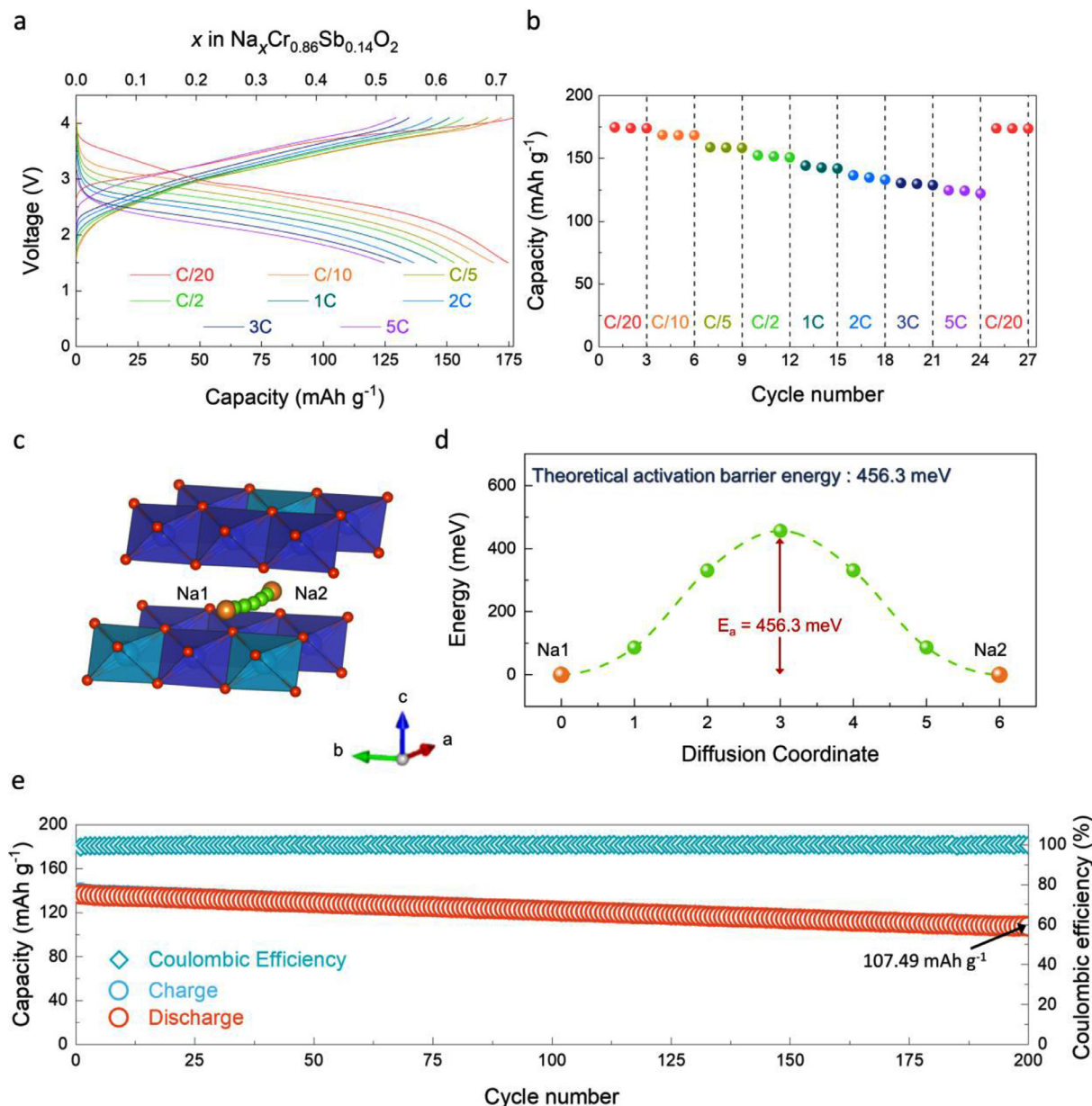


Fig. 5. (a) Charge/discharge profiles of O₃-Na_xCr_{0.86}Sb_{0.14}O₂ at various current densities. (b) power capability of O₃-Na_xCr_{0.86}Sb_{0.14}O₂ at various current densities. (c) predicted Na⁺-ion diffusion motion in O₃-Na_{0.72}Cr_{0.86}Sb_{0.14}O₂ and (d) predicted activation barrier energy for Na⁺-ion diffusion in O₃-Na_{0.72}Cr_{0.86}Sb_{0.14}O₂. (e) charge/discharge capacity and coulombic efficiency of O₃-Na_{0.72}Cr_{0.86}Sb_{0.14}O₂ over 200 cycles at 2C.

suppressed Cr migration to Na layers even after charging to 4.1 V (vs. Na⁺/Na) enables better power-capability of O₃-Na_{0.72}Cr_{0.86}Sb_{0.14}O₂ relative to that of O₃-NaCrO₂. In addition, using the nudged elastic band (NEB) method based on first-principles calculation, we predicted the theoretical activation barrier energy for Na⁺ diffusion in Na_{0.72}Cr_{0.86}Sb_{0.14}O₂. As shown in Fig. 5c and d, it was verified that only ~456.3 meV is required for the Na⁺ diffusion, indicating facile Na⁺ diffusion in the Na_{0.72}Cr_{0.86}Sb_{0.14}O₂ structure. In addition, we performed the additional electrochemical tests of Na_{0.72}Cr_{0.86}Sb_{0.14}O₂ at the various current rate of 5C at 10, 15, 20, 25 and 30C (Fig. S11), which indicates that the power-capability of Na_{0.72}Cr_{0.86}Sb_{0.14}O₂ at the very high current densities is not better than the reported Cr-based layered oxide cathode materials [22,28,38]. It was supposed that the reason on the poor power-capability of Na_{0.72}Cr_{0.86}Sb_{0.14}O₂ is due to the relatively large structural change by enlargement of available Na contents in the structure during charge/discharge. The available

Na contents of the reported Cr-based layered oxide cathode materials are less than ~0.55 mol, which is smaller than the available Na contents of Na_{0.72}Cr_{0.86}Sb_{0.14}O₂ (~0.72 mol). Thus, Na_{0.72}Cr_{0.86}Sb_{0.14}O₂ experiences larger volume change during charge/discharge than the reported Cr-based layered oxide cathode materials, which may result in the relatively poor power-capability and kinetics for Na⁺ diffusion in the Na_{0.72}Cr_{0.86}Sb_{0.14}O₂ structures during charge/discharge with the high current densities, despite the large available capacity and Na contents. In terms of the cycle performance, Na_{0.72}Cr_{0.86}Sb_{0.14}O₂ exhibited outstanding capacity retention of ~78.64% compared with the initial capacity for 200 cycles at 2C, with a high coulombic efficiency of >99% (Fig. 5e). In addition, we compared the available capacities among O₃-Na_{0.72}Cr_{0.86}Sb_{0.14}O₂ and other Cr-based layered oxide cathode materials for Na-ion batteries. As tabulated in Table 1 [22,28,38–40], it was identified that O₃-Na_{0.72}Cr_{0.86}Sb_{0.14}O₂ exhibits not only the largest available capacity with high coulombic efficiency but also outstanding

Table 1

Comparing the available capacities among O3-Na_{0.72}Cr_{0.86}Sb_{0.14}O₂ and other Cr-based layered oxide cathode materials for Na-ion batteries.

Cr-based Layered-oxide cathode	Voltage range [V vs. Na ⁺ /Na]	Charge/Discharge Capacity [mAh g ⁻¹]	Refs.
Na _{0.72} Cr _{0.86} Sb _{0.14} O ₂	1.5–4.1	Ch : 176.86 Dis : 174.69	This work
NaCrO ₂	2.0–3.6	Ch : 127 Dis : 121	[22]
Na _{0.95} CrO ₂	2.0–4.0	Ch : 107 Dis : 101	[39]
Na _{0.95} Cr _{0.95} Ti _{0.05} O ₂	2.3–3.6	Ch : 106.1 Dis : 104	[40]
Na _{0.9} Ca _{0.035} Cr _{0.97} Ti _{0.03} O ₂	1.5–3.8	Ch : 144.8 Dis : 136.1	[28]
Na _{0.88} Cr _{0.88} Ru _{0.12} O ₂	1.5–3.8	Ch : 159 Dis : 156	[38]

electrochemical stability even at a high charge cut-off voltage of 4.1 V (vs. Na⁺/Na).

The reaction mechanism of Na_{0.72}Cr_{0.86}Sb_{0.14}O₂ during charge/discharge was investigated using *ex-situ* X-ray absorption near edge structure (XANES) analysis. As shown in Fig. 6a, the Cr K-edge of O3-Na_{0.72}Cr_{0.86}Sb_{0.14}O₂ shifted toward lower energy level during charge with growth of the pre-edge and returned to the original state after discharge, which indicates the occurrence of reversible Cr³⁺/Cr⁴⁺ redox reaction at O3-Na_{0.72}Cr_{0.86}Sb_{0.14}O₂ during Na⁺ de/intercalation. The Cr³⁺/Cr⁴⁺ redox reaction was also confirmed through comparison of the integrated spin moments of Na_{0.75}Cr_{0.86}Sb_{0.14}O₂ and Na₀Cr_{0.86}Sb_{0.14}O₂ predicted by first-principles calculation (Fig. 6b). It was verified that the total spin moments of the Cr ion on Na_{0.75}Cr_{0.86}Sb_{0.14}O₂ and Na₀Cr_{0.86}Sb_{0.14}O₂ are close to approximately 3 and 2, respectively, which implies that the valence state of Cr ions on Na_{0.75}Cr_{0.86}Sb_{0.14}O₂ and Na₀Cr_{0.86}Sb_{0.14}O₂ are +3 and +4, respectively. In addition, we investigated the change of local environments of Na_{0.72}Cr_{0.86}Sb_{0.14}O₂ during charge/discharge using extended X-ray absorption fine structure (EXAFS) analysis (Fig. 6c). In terms of pristine Na_{0.72}Cr_{0.86}Sb_{0.14}O₂, the Cr–O and Cr–Cr (or Sb) bond lengths were close to 1.59 and 2.56 Å, respectively. After charging to 4.1 V (vs. Na⁺/Na), the bond lengths decreased to 1.53 and 2.52 Å, which results from oxidation from Cr³⁺ to Cr⁴⁺. In particular, they returned to the original bond lengths after discharging to 1.5 V (vs. Na⁺/Na), indicating the high structural reversibility of Na_{0.72}Cr_{0.86}Sb_{0.14}O₂ during 0.72 mol Na⁺ deintercalation accompanying the O3–P3 phase transition. Moreover, these EXAFS results are well matched with the theoretical local environments on Cr–O bonding in CrO₆ octahedra of Na_{0.75}Cr_{0.86}Sb_{0.14}O₂ and Na₀Cr_{0.86}Sb_{0.14}O₂ predicted by first-principles calculation (Fig. 6d).

3. Conclusion

In this work, we demonstrated that the reversibly available capacity of O3-NaCrO₂ can be enhanced by substitution of > 0.14 mol Sb⁵⁺ in the structure. O3-Na_{0.72}Cr_{0.86}Sb_{0.14}O₂ delivered a large specific capacity of ~175 mAh g⁻¹, corresponding to ~0.72 mol Na⁺ de/intercalation, in the voltage range of 1.5–4.1 V (vs. Na⁺/Na), and its initial coulombic efficiency was as high as ~98.7%. This electrochemical performance clearly differed from that of O3-NaCrO₂ measured under the same conditions (small specific capacity of ~80 mAh g⁻¹ with poor initial coulombic efficiency of 37.04%). Through first-principles calculation, it was verified that the presence of > 0.14 mol Sb⁵⁺ in the NaCrO₂ structure results in thermodynamic instability of Cr migration to the Na layers even after full Na⁺ deintercalation from the structure. Moreover, *operando* XRD and HAADF-STEM analyses revealed reversible O3–P3 phase transition without the formation of the irreversible O3' phase and the direct visualization of the non-occurrence of Cr migration to the Na layers after the charge/discharge cycling, which is consistent with the computational simulation results. As a promising cathode material for NIBs, O3-Na_{0.72}Cr_{0.86}Sb_{0.14}O₂ delivered a specific capacity of ~124.56 mA g⁻¹, corresponding to 71.31% of the capacity measured at C/20. Through first-principles calculation, it was confirmed that the outstanding power-capability of O3-Na_{0.72}Cr_{0.86}Sb_{0.14}O₂ originates from the low activation barrier energy required for facile Na⁺ diffusion. Furthermore, for 200 cy-

cles, the specific capacity of O3-Na_{0.72}Cr_{0.86}Sb_{0.14}O₂ was maintained up to ~78.64% compared with the initial capacity, with a high coulombic efficiency of >99%. We expect these findings can provide guidelines for enhancing the poor electrochemical performance of electrode materials suffering from irreversible structural change during charge/discharge for not only NIBs but also other rechargeable batteries.

4. Experimental

4.1. Synthesis process of O3-Na_{1-2x}Cr_{1-x}Sb_xO₂

To synthesize O3-Na_{1-2x}Cr_{1-x}Sb_xO₂, Na₂CO₃ (purity: 99.5%), Cr₂O₃ (purity: 99.5%), and CrSbO₄ were used as precursors. The precursors were weighed in the desired ratios and mixed using a planetary ball-mill at 500 rpm for 12 h. After mixing, the mixture was pressed into a pellet and heated directly at 900 °C for 10 h in Ar [22,41]. The color of the O3-Na_{1-2x}Cr_{1-x}Sb_xO₂ was light green.

In this synthesis system, if antimony oxide is used instead of CrSbO₄, it is not doped and reacts separately with sodium because the reactivity of chromium oxide is low [41]. As a result, CrSbO₄ was used as a precursor. To prepare CrSbO₄, Cr₂O₃ and Sb₂O₄ (Sb(III) + Sb(V)) were used, and Sb₂O₄ (Sb(III) + Sb(V)) was obtained by heat treatment of Sb₂O₃ (purity: 99.5%) at 550 °C for 10 h in air. Then, Cr₂O₃ and Sb₂O₄ in a 1:1 molar ratio were mixed using high-energy ball-milling at 400 rpm for 12 h, and the mixture was heated at 600 °C for 3 h and 1050 °C for 10 h in air.

4.2. Materials characterization

The crystal structure and information of Na_{1-2x}Cr_{1-x}Sb_xO₂ was analyzed using XRD (PANalytical Empyrean) with Cu K α radiation ($\lambda = 1.54178$ Å), and structural data were collected over the 2θ range of 10°–50° and 10°–80° with a step size of 0.01° Rietveld refinement was performed using FullProf software. The microstructure of each sample was examined using field-emission scanning electron microscopy (FE-SEM; SU-8010, Hitachi) at an accelerating voltage of 15 kV. High-resolution transmission electron microscopy (HR-TEM; JEM-F200 at the National Center for Inter-university Research Facilities (NCIRF) at Seoul National University) at accelerating voltages of 80–120 kV; elemental mapping was also performed using energy-dispersive X-ray spectroscopy (EDS) and high-angle annular dark-field scanning transmission electron microscopy (HAADF-STEM) and bright-field scanning transmission electron microscopy (BF-STEM) (FEI, TITAN TM 80–300 STEM at Korea Institute of Science and Technology (KIST)) at accelerating voltages of 300 keV; the d-spacing was obtained using a Cs-corrected microscope. *Operando* XRD pattern was used to investigate the structural evolution during discharging at the 3D XRS beamline at the Pohang Accelerator Laboratory (PAL). The Cr K-edge XAS spectra were obtained at beamline 10C at the PAL using Cr metal foils as references.

4.3. Electrochemical characterization

To increase the electronic conductivity, the as-synthesized O3-Na_{1-2x}Cr_{1-x}Sb_xO₂ powder was mixed with pyromellitic acid (C₁₀H₆O₂, 96%: PA) as the carbon source for carbonization, and the weight ratio

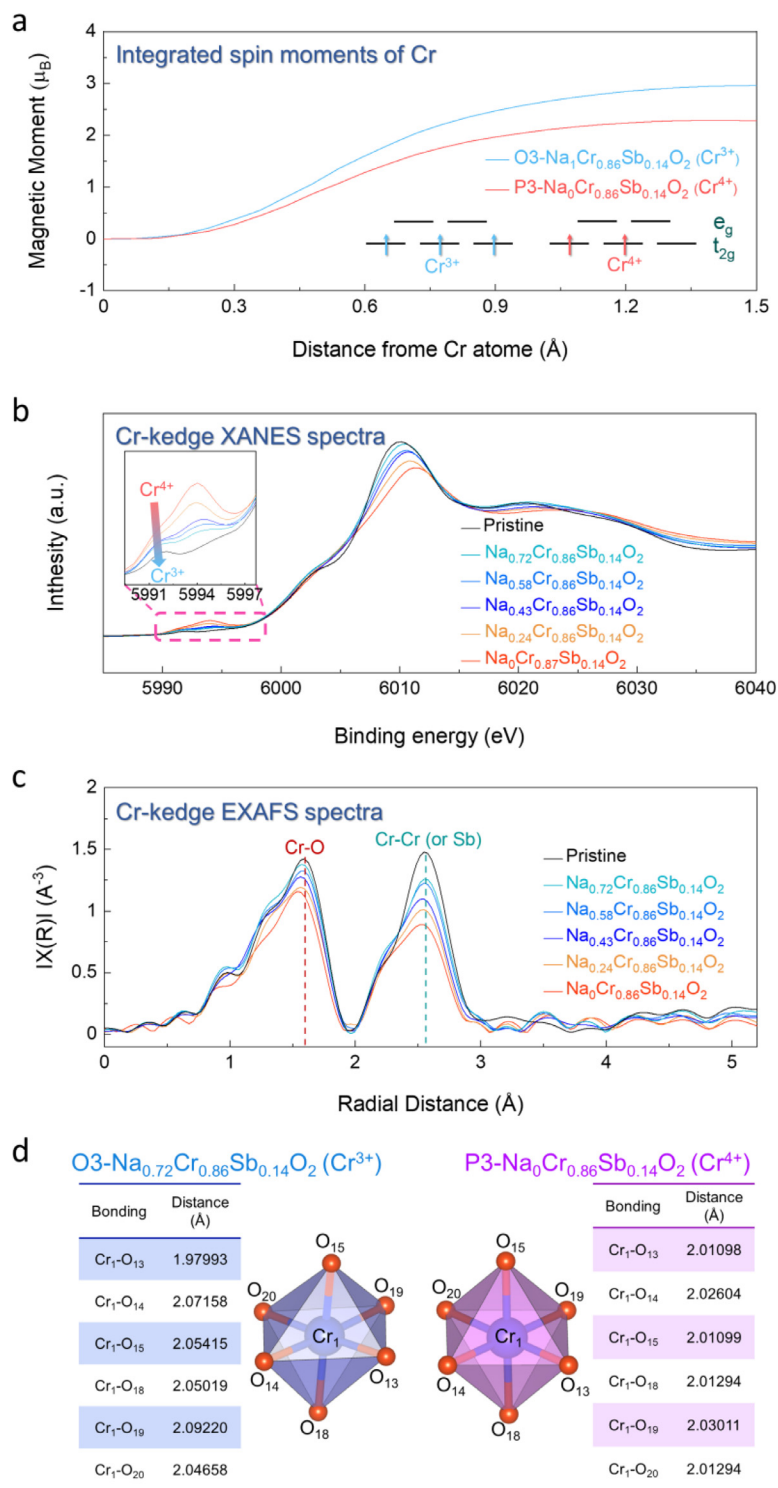


Fig. 6. (a) Integrated spin moments of O3-Na₁Cr_{0.86}Sb_{0.14}O₂ (Cr³⁺) and P3-Na₀Cr_{0.86}Sb_{0.14}O₂ (Cr⁴⁺). *Ex-situ* Cr K-edge (b) XANES spectra and (c) EXAFS spectra of Na_xCr_{0.86}Sb_{0.14}O₂ (0 ≤ x ≤ 0.72). (d) comparison of predicted Cr–O bond distances of CrO₆ in O3-Na_{0.72}Cr_{0.86}Sb_{0.14}O₂ and P3-Na₀Cr_{0.86}Sb_{0.14}O₂ through first-principles calculation.

of the powder and PA was 85:15. After mixing, a pellet was formed using the mixture and then heated at 550 °C for 30 min in Ar. Moreover, to enhance the preparation of the electrode, carbonized active material, Super-P, and polyvinylidene fluoride (PVDF) in a 8:1:1 wt ratio was mixed with N-methyl-2-pyrrolidone using a mortar and pestle. The mixed slurry was applied onto Al foil to a thickness of 200 μm and dried in an oven at 100 °C. The dried electrode was punched into disks of 10π-mm diameter. The mass loading was ~2.0 × 10⁻³ g cm⁻², and the total active material content was ~68 wt%. The coin cells were as-

sembled as half-cells using Na metal as the counter electrode, Whatman GF/F glass fiber filter as the separator, and 0.5 M NaPF₆ in a 97:3 v/v mixture of polyethylene carbonate and fluoroethylene carbonate (FEC) as the electrolyte. Electrochemical characterization was performed using 2030-type coin cells assembled in an Ar-filled glove-box. Power capability tests were performed at various C-rates (C/20, C/10, C/5, C/2, 1C, 2C, 3C, and 5C) in the voltage range of 1.5–4.1 V using an automatic battery charge/discharge test system (WBCS 3000, WonATech).

4.4. Computational details

All the density functional theory (DFT) calculations were performed using the Vienna Ab initio Simulation Package (VASP) and projector-augmented wave (PAW) pseudopotentials with a plane-wave basis set, as implemented in VASP [42]. Perdew–Burke–Ernzerhof (PBE) parametrization of the generalized gradient approximation (GGA) was used for the exchange correlation functional [43,44]. Detailed information for the DFT calculations is as follows: the k-point grid was $2 \times 3 \times 1$ and the supercell structure of $\text{Na}_x\text{Cr}_{0.86}\text{Sb}_{0.14}\text{O}_2$ was $2 \times 2 \times 1$.

The GGA + U method was adopted to address the localization of the d-orbital in Cr ions, with a U_{eff} value of 3.7 eV, as used in previous studies [17,45]. A kinetic energy cutoff of 500 eV was used in all the calculations, and all the structures were optimized until the force in the unit cell converged to within $0.03 \text{ eV } \text{\AA}^{-1}$.

CASM software was used to generate all the Na^+ /vacancy configurations for each composition, followed by full DFT calculations on a maximum of 20 configurations with the lowest electrostatic energy for each composition used to obtain the convex-hull plot of $\text{Na}_x\text{Cr}_{0.86}\text{Sb}_{0.14}\text{O}_2$ [46].

NEB calculations were performed to determine the activation barrier for Na^+ diffusion in the $\text{Na}_x\text{Cr}_{0.86}\text{Sb}_{0.14}\text{O}_2$ structure [47]. To perform the calculations, five intermediate images were generated between each Na site. These structures were then calculated using the NEB algorithm with fixed lattice parameters and free internal atomic positions. The schematic illustrations, crystal structure with BVOL, and NEB calculation results for Na^+ diffusion pathways were drawn using VESTA software.

Declaration of Competing Interest

The authors declare that they have no known competing financial interests or personal relationships that could have appeared to influence the work reported in this paper.

CRedit authorship contribution statement

Wonseok Ko: Conceptualization, Validation, Investigation, Resources, Writing – original draft, Writing – review & editing, Visualization, Data curation. **Min-Kyung Cho:** Validation, Formal analysis. **Jungmin Kang:** Investigation, Validation. **Hyunyoung Park:** Software. **Jinho Ahn:** Investigation. **Yongseok Lee:** Investigation. **Seokjin Lee:** Investigation. **Sangyeop Lee:** Validation. **Kwang Heo:** Conceptualization. **Jihyun Hong:** Investigation, Resources. **Jung-Keun Yoo:** Conceptualization. **Jongsoon Kim:** Project administration, Supervision, Visualization, Writing – review & editing, Funding acquisition.

Acknowledgements

This research was supported by the National Research Foundation of Korea funded by the Ministry of Science and ICT of Korea (NRF-2021R1A2C1014280, NRF-2020M2D8A2070870, NRF-2019M3D1A2104105), and the Korea Institute of Materials Science of the Republic of Korea (PNK7330). The calculation resources were supported by the Supercomputing Center in Korea Institute of Science and Technology Information (KSC-2019-CRE-0215).

Supplementary materials

Supplementary material associated with this article can be found, in the online version, at doi:10.1016/j.ensm.2022.01.023.

References

[1] S. Davidsson Kurland, Energy use for GWh-scale lithium-ion battery production, Environ. Res. Commun. 2 (2019) 012001, doi:10.1088/2515-7620/ab5e1e.

[2] W. Zhang, A. Maleki, A.K. Birjandi, M. Alhuyi Nazari, O. Mohammadi, Discrete optimization algorithm for optimal design of a solar/wind/battery hybrid energy conversion scheme, Int. J. Low Carbon Technol. 16 (2021) 326–340, doi:10.1093/ijlct/ctaa067.

[3] C.P. Grey, G. Ceder, K. Kang, Y.S. Meng, J. Bre'ger, Electrodes with high power and high capacity for rechargeable lithium batteries, Science 311 (2006) 977–980 (80-), doi:10.1126/science.1122152.

[4] H. Kwak, D. Han, J. Lyoo, J. Park, S.H. Jung, Y. Han, G. Kwon, H. Kim, S. Hong, K. Nam, Y.S. Jung, New cost-effective halide solid electrolytes for all-solid-state batteries: mechanochemically prepared Fe^{3+} -substituted Li_2ZrCl_6 , Adv. Energy Mater. 11 (2021) 2003190, doi:10.1002/aenm.202003190.

[5] K.T. Kim, D.Y. Oh, S. Jun, Y.B. Song, T.Y. Kwon, Y. Han, Y.S. Jung, Tailoring slurries using cosolvents and li salt targeting practical all-solid-state batteries employing sulfide solid electrolytes, Adv. Energy Mater. (2021) 2003766 2003766, doi:10.1002/aenm.202003766.

[6] H. He, H. Tong, X. Song, X. Song, J. Liu, Highly stable Zn metal anodes enabled by atomic layer deposited Al_2O_3 coating for aqueous zinc-ion batteries, J. Mater. Chem. A. 8 (2020) 7836–7846, doi:10.1039/D0TA00748J.

[7] J. Kim, H. Kim, S. Lee, High power cathode material $\text{Na}_4\text{VO}(\text{PO}_4)_2$ with open framework for Na ion batteries, Chem. Mater. 29 (2017) 3363–3366, doi:10.1021/acs.chemmater.6b04557.

[8] N. Yabuuchi, M. Kajiyama, J. Iwatate, H. Nishikawa, S. Hitomi, R. Okuyama, R. Usui, Y. Yamada, S. Komaba, P2-type $\text{Na}[\text{Fe}_{1/2}\text{Mn}_{1/2}]\text{O}_2$ made from earth-abundant elements for rechargeable Na batteries, Nat. Mater. 11 (2012) 512–517, doi:10.1038/nmat3309.

[9] J. Wang, H. Wu, Y. Cui, S. Liu, X. Tian, Y. Cui, X. Liu, Y. Yang, A new class of ternary compound for lithium-ion battery: from composite to solid solution, ACS Appl. Mater. Interfaces 10 (2018) 5125–5132, doi:10.1021/acsami.7b15494.

[10] R.A. Shakoob, D.H. Seo, H. Kim, Y.U. Park, J. Kim, S.W. Kim, H. Gwon, S. Lee, K. Kang, A combined first principles and experimental study on $\text{Na}_3\text{V}_2(\text{PO}_4)_2\text{F}_3$ for rechargeable Na batteries, J. Mater. Chem. 22 (2012) 20535–20541, doi:10.1039/c2jm33862a.

[11] K.T. Kim, C.Y. Yu, C.S. Yoon, S.J. Kim, Y.K. Sun, S.T. Myung, Carbon-coated $\text{Li}_4\text{Ti}_5\text{O}_{12}$ nanowires showing high rate capability as an anode material for rechargeable sodium batteries, Nano Energy 12 (2015) 725–734, doi:10.1016/j.nanoen.2015.01.034.

[12] J. Kim, D.H. Seo, H. Kim, I. Park, J.K. Yoo, S.K. Jung, Y.U. Park, W.A. Goddard, K. Kang, Unexpected discovery of low-cost maricite NaFePO_4 as a high-performance electrode for Na-ion batteries, Energy Environ. Sci. 8 (2015) 540–545, doi:10.1039/c4ee03215b.

[13] J. Kim, I. Park, H. Kim, K.Y. Park, Y.U. Park, K. Kang, Tailoring a new 4V-class cathode material for Na-ion batteries, Adv. Energy Mater. 6 (2016) 1502147, doi:10.1002/aenm.201502147.

[14] W. Hong, Y. Zhang, L. Yang, Y. Tian, P. Ge, J. Hu, W. Wei, G. Zou, H. Hou, X. Ji, Carbon quantum dot micelles tailored hollow carbon anode for fast potassium and sodium storage, Nano Energy 65 (2019) 104038, doi:10.1016/j.nanoen.2019.104038.

[15] Y. Liu, Z. Tai, Q. Zhang, H. Wang, W.K. Pang, H.K. Liu, K. Konstantinov, Z. Guo, A new energy storage system: Rechargeable potassium-selenium battery, Nano Energy. 35 (2017) 36–43. 10.1016/j.nanoen.2017.03.029.

[16] H. Kim, H. Kim, Z. Ding, M.H. Lee, K. Lim, G. Yoon, K. Kang, Recent progress in electrode materials for sodium-ion batteries, Adv. Energy Mater. 6 (2016) 1–38, doi:10.1002/aenm.201600943.

[17] W. Ko, J.K. Yoo, H. Park, Y. Lee, I. Kang, J. Kang, J.H. Jo, J.U. Choi, J. Hong, S.T. Myung, J. Kim, Exceptionally high-energy tunnel-type $\text{V}_{1.5}\text{Cr}_{0.5}\text{O}_{4.5}\text{H}$ nanocomposite as a novel cathode for Na-ion batteries, Nano Energy 77 (2020) 105175, doi:10.1016/j.nanoen.2020.105175.

[18] Y. Fang, X.Y. Yu, X.W.D. Lou, Nanostructured electrode materials for advanced sodium-ion batteries, Matter 1 (2019) 90–114, doi:10.1016/j.matt.2019.05.007.

[19] R.J. Clément, J. Billaud, A. Robert Armstrong, G. Singh, T. Rojo, P.G. Bruce, C.P. Grey, Structurally stable Mg-doped $\text{P2-Na}_{2/3}\text{Mn}_{1/3}\text{yMgyO}_2$ sodium-ion battery cathodes with high rate performance: insights from electrochemical, NMR and diffraction studies, Energy Environ. Sci. 9 (2016) 3240–3251, doi:10.1039/c6ee01750a.

[20] K. Amaha, W. Kobayashi, S. Akama, K. Mitsuishi, Y. Moritomo, Interrelation between inhomogeneity and cyclability in $\text{O}_3\text{-NaFe}_{1/2}\text{Co}_{1/2}\text{O}_2$, Phys. Status Solidi Rapid Res. Lett. 11 (2017) 1600284, doi:10.1002/pssr.201600284.

[21] H. Park, Y. Lee, M. Cho, J. Kang, W. Ko, Y.H. Jung, T.-Y. Jeon, J. Hong, H. Kim, S.-T. Myung, J. Kim, $\text{Na}_2\text{Fe}_2\text{F}_7$: a fluoride-based cathode for high power and long life Na-ion batteries, Energy Environ. Sci. 14 (2021) 1469–1479, doi:10.1039/D0EE02803G.

[22] C.Y. Yu, J.S. Park, H.G. Jung, K.Y. Chung, D. Aurbach, Y.K. Sun, S.T. Myung, NaCrO_2 cathode for high-rate sodium-ion batteries, Energy Environ. Sci. 8 (2015) 2019–2026, doi:10.1039/c5ee00695c.

[23] T. Ohzuku, A. Ueda, M. Nagayama, Y. Iwakoshi, H. Komori, Comparative study of LiCoO_2 , $\text{LiNi}_{1/2}\text{Co}_{1/2}\text{O}_2$ and LiNiO_2 for 4 volt secondary lithium cells, Electrochim. Acta 38 (1993) 1159–1167, doi:10.1016/0013-4686(93)80046-3.

[24] K. OZAWA, Lithium-ion rechargeable batteries with LiCoO_2 and carbon electrodes: the LiCoO_2/C system, Solid State Ion. 69 (1994) 212–221, doi:10.1016/0167-2738(94)90411-1.

[25] A.O. Kondrakov, A. Schmidt, J. Xu, H. Geßwein, R. Mönig, P. Hartmann, H. Sommer, T. Brezesinski, J. Janek, Anisotropic lattice strain and mechanical degradation of high- and low-nickel NCM cathode materials for Li-ion batteries, J. Phys. Chem. C 121 (2017) 3286–3294, doi:10.1021/acs.jpcc.6b12885.

[26] S. Liu, L. Xiong, C. He, Long cycle life lithium ion battery with lithium nickel

- cobalt manganese oxide (NCM) cathode, *J. Power Sources* 261 (2014) 285–291, doi:10.1016/j.jpowsour.2014.03.083.
- [27] K. Kubota, I. Ikeuchi, T. Nakayama, C. Takei, N. Yabuuchi, H. Shiiba, M. Nakayama, S. Komaba, New insight into structural evolution in layered NaCrO_2 during electrochemical sodium extraction, *J. Phys. Chem. C* 119 (2015) 166–175, doi:10.1021/jp5105888.
- [28] I. Lee, G. Oh, S. Lee, T.Y. Yu, M.H. Alfaruqi, V. Mathew, B. Sambandam, Y.K. Sun, J.Y. Hwang, J. Kim, Cationic and transition metal co-substitution strategy of O3-type NaCrO_2 cathode for high-energy sodium-ion batteries, *Energy Storage Mater.* (2021), doi:10.1016/j.ensm.2021.05.046.
- [29] J. Rodríguez-Carvajal, Recent advances in magnetic structure determination by neutron powder diffraction, *Physica B Condens. Matter* 192 (1–2) (1993) 55–69, doi:10.1016/0921-4526(93)90108-1.
- [30] S. Adams, Modelling ion conduction pathways by bond valence pseudopotential maps, *Solid State Ion.* 136–137 (2000) 1351–1361, doi:10.1016/S0167-2738(00)00576-2.
- [31] W. Ko, J.K. Yoo, H. Park, Y. Lee, H. Kim, Y. Oh, S.T. Myung, J. Kim, Development of $\text{Na}_2\text{FePO}_4\text{F}$ /conducting-polymer composite as an exceptionally high performance cathode material for Na-ion batteries, *J. Power Sources* 432 (2019) 1–7, doi:10.1016/j.jpowsour.2019.05.066.
- [32] W.B. Park, M.G.T. Nathan, S.C. Han, J.W. Lee, K.S. Sohn, M. Pyo, Alivalent-doped sodium chromium oxide ($\text{Na}_{0.9}\text{Cr}_{0.9}\text{Sn}_{0.1}\text{O}_2$ and $\text{Na}_{0.8}\text{Cr}_{0.9}\text{Sb}_{0.1}\text{O}_2$) for sodium-ion battery cathodes with high-voltage characteristics, *RSC Adv.* 10 (2020) 43273–43281, doi:10.1039/D0RA08332A.
- [33] C. Zhao, Q. Wang, Z. Yao, J. Wang, B. Sánchez-Lengeling, F. Ding, X. Qi, Y. Lu, X. Bai, B. Li, H. Li, A. Aspuru-Guzik, X. Huang, C. Delmas, M. Wagemaker, L. Chen, Y.S. Hu, Rational design of layered oxide materials for sodium-ion batteries, *Science* 370 (2020) 708–711 (80-), doi:10.1126/science.aay9972.
- [34] P. GE, Electrochemical intercalation of sodium in graphite, *Solid State Ion.* 28–30 (1988) 1172–1175, doi:10.1016/0167-2738(88)90351-7.
- [35] D. Eum, B. Kim, S.J. Kim, H. Park, J. Wu, S.P. Cho, G. Yoon, M.H. Lee, S.K. Jung, W. Yang, W.M. Seong, K. Ku, O. Tamwattana, S.K. Park, I. Hwang, K. Kang, Voltage decay and redox asymmetry mitigation by reversible cation migration in lithium-rich layered oxide electrodes, *Nat. Mater.* 19 (2020) 419–427, doi:10.1038/s41563-019-0572-4.
- [36] J. Ahn, J. Kang, M. Cho, H. Park, W. Ko, Y. Lee, H. Kim, Y.H. Jung, T. Jeon, H. Kim, W. Ryu, J. Hong, J. Kim, Selective anionic redox and suppressed structural disorder enabling high-energy and long-life Li-rich layered-oxide cathode, *Adv. Energy Mater.* (2021) 2102311 2102311, doi:10.1002/aenm.202102311.
- [37] T. Aoki, M.R. McCartney, D.J. Smith, Large-collection-angle BF STEM imaging of compound semiconductors, *Microsc. Microanal.* 21 (2015) 1921–1922, doi:10.1017/S1431927615010387.
- [38] K. Xi, S. Chu, X. Zhang, X. Zhang, H. Zhang, H. Xu, J. Bian, T. Fang, S. Guo, P. Liu, M. Chen, H. Zhou, A high-performance layered Cr-based cathode for sodium-ion batteries, *Nano Energy* 67 (2020) 104215, doi:10.1016/j.nanoen.2019.104215.
- [39] K. Mathiyalagan, A. Ponnaiah, K. Karuppiah, S. Rengapillai, S. Marimuthu, Enhanced performance on layered O3- $\text{Na}_{0.95}\text{CrO}_2$ cathode material for emerging sodium-ion batteries, *Ionics* 26 (2020) 3929–3936 (Kiel), doi:10.1007/s11581-020-03523-7.
- [40] W. Li, Y. Wang, G. Hu, Z. Peng, Y. Cao, Y. Zeng, K. Du, Ti-doped NaCrO_2 as cathode materials for sodium-ion batteries with excellent long cycle life, *J. Alloy. Compd.* 779 (2019) 147–155, doi:10.1016/j.jallcom.2018.11.257.
- [41] A.A. Pospelov, V.B. Nalbandyan, Preparation, crystal structures and rapid hydration of P2- and P3-type sodium chromium antimony oxides, *J. Solid State Chem.* 184 (2011) 1043–1047, doi:10.1016/j.jssc.2011.03.011.
- [42] H. He, D. Huang, Y. Tang, Q. Wang, X. Ji, H. Wang, Z. Guo, Tuning nitrogen species in three-dimensional porous carbon via phosphorus doping for ultra-fast potassium storage, *Nano Energy* 57 (2019) 728–736, doi:10.1016/j.nanoen.2019.01.009.
- [43] P.E. Blöchl, Projector augmented-wave method, *Phys. Rev. B* 50 (1994) 17953–17979, doi:10.1103/PhysRevB.50.17953.
- [44] J.P. Perdew, K. Burke, M. Ernzerhof, Generalized gradient approximation made simple, *Phys. Rev. Lett.* 77 (1996) 3865–3868, doi:10.1103/PhysRevLett.77.3865.
- [45] V.I. Anisimov, F. Aryasetiawan, A.I. Lichtenstein, First-principles calculations of the electronic structure and spectra of strongly correlated systems: the LDA + U method, *J. Phys. Condens. Matter* 9 (1997) 767–808, doi:10.1088/0953-8984/9/4/002.
- [46] G. Henkelman, B.P. Uberuaga, H. Jónsson, A climbing image nudged elastic band method for finding saddle points and minimum energy paths, *J. Chem. Phys.* 113 (2000) 9901–9904, doi:10.1063/1.1329672.
- [47] J. Kang, H. Park, H. Kim, J.H. Jo, W. Ko, Y. Lee, S.T. Myung, J. Kim, Development of a new mixed-polyanion cathode with superior electrochemical performances for Na-ion batteries, *ACS Sustain. Chem. Eng.* 8 (2020) 163–171, doi:10.1021/acsschemeng.9b04944.